Hindawi
International Journal of Aerospace Engineering
Volume 2019, Article ID 2702057, 17 pages
https://doi.org/10.1155/2019/2702057

Research Article

Method for Predicting the Liquid-Sloshing Characteristics of a Microsatellite Propulsion System

L. Teng, T. Meng, and Zh. H. Jin

School of Aeronautics and Astronautics, Zhejiang University, Hangzhou 310027, China

Correspondence should be addressed to T. Meng; mengtao@zju.edu.cn

Received 8 June 2018; Revised 12 September 2018; Accepted 9 October 2018; Published 3 February 2019

Academic Editor: Giulio Avanzini

In this study, a method for establishing a prediction model for the liquid-sloshing characteristics of microsatellite propulsion systems is proposed. The ideal states of the liquid-sloshing characteristics are considered for the following three models: (1) storage tank, (2) coupled storage tank and microsatellite, and (3) coupled storage tank and microsatellite with a deployment mechanism. The smoothed-particle hydrodynamics method is implemented in ABAQUS to study the effect of sloshing on a storage tank and microsatellite disturbance for the above three cases. Relationship models between the sloshing time, sloshing angular velocity, amount of fluid filled, and satellite attitude angular velocity are established. The analysis results show that the disturbance angular velocity of the empty storage tank and sloshing angular velocity have a linear relationship. Furthermore, the disturbance angular velocity of the liquid-filled storage tank exhibits a surface relationship with the sloshing angular velocity and amount of fluid filled in a three-dimensional coordinate system. Additionally, the disturbance angular velocity in the liquid-filled state of the storage tank is higher than that of the empty storage tank, and the degree of disturbance decreases with the increase in the mass of the coupling. The disturbance of the storage tank and microsatellite with the deployment mechanism is 10^{-2°/s when the angular velocities of the satellite are $\omega_x' = 3$, $\omega_y' = 3$, and $\omega_z' = 2$. The maximum and minimum deviations between the calculation and simulation results of the three models are 7.6% and 1.1%, respectively. The model is used to predict the disturbance angular velocity of the microsatellite. When the calculation results of the model are compared with the orbit satellite data, the maximum and minimum disturbance angular velocity deviations occur in the y and z directions with a deviation of 43.36% and 14.86%, respectively. This demonstrates the accuracy of the analysis and model. The results of this study can provide theoretical guidance for the engineering design and attitude and orbital control of a microsatellite propulsion system.

1. Introduction

The continuous improvement of modern technology has led to several important developments such as microelectronics, microcomputers, and new material development. Although large-satellite technology is advancing, the function and integration of microsatellites have gained increasing attention. Research in the field of space pertaining to modern microsatellites is rapidly expanding owing to several attractive features, including their low weight, small size, low cost, high performance, and short development period. Presently, the development of microsatellites is focused on network applications. Satellite formations or constellations consist of several small satellites, and thus, each satellite requires precise control of its orbit phase and attitude. In addition, because microsatellites are being used for increasingly difficult tasks, their pointing accuracy and precision have improved at a rapid rate. Furthermore, the demand for in-orbit propulsion technology of microsatellites has heightened along with that for miniaturized propulsion systems. The propulsion systems of microsatellites have the characteristics of high-volume utilization, high efficiency, adept control, and less environmental pollution. Specifically, the structure of a liquid micropropulsion system is relatively simple and has the desirable characteristics of low power consumption and high specific impulse. Thus, liquid

micropropulsion systems have become the most common microsatellite propulsion systems.

The liquid propulsion system of a microsatellite is an important component [1] having a direct effect on the operating life, reliability, orbit and attitude control, maneuverability, and position retention of the microsatellite. With the development of microsatellites, users are demanding improved satellite attitude and orbit control. However, instantaneous attitude and orbit adjustments lead to liquid sloshing in the storage tank of a satellite propulsion system. The dynamic characteristics of a storage tank will affect those of the satellite [2, 3], which in turn affect the stability and control precision of the motion system. Studying the sloshing characteristics of a liquid storage tank also requires understanding the effect of the liquid sloshing on the attitude and tracking control of the storage tank structure, which will assist in improving the control precision and capability.

The occurrence of liquid sloshing in storage tanks is a concern across many fields such as aerospace, nautical science, and automotive engineering. Understanding the sloshing characteristics of storage tanks is essential for scientific research and engineering design. The smoothed-particle hydrodynamics (SPH) method is a Lagrange-type mesh-less method used to numerically simulate fluid dynamics. This method uses the kernel function to approximately describe the differential equation. There is no grid relation between the particles, and the value of a given point is locally approximated by its neighborhood node. This method is suitable for dealing with large deformations and fluid–solid coupling problems. Ni et al. [4] and Liu and Chang [5] studied the SPH method, and the findings showed that regular, uniform particle distributions yield more accurate results and increased the stability of the numerical calculations. Gingold and Monaghan [6] and Lucy [7] first proposed the SPH method and discussed its application in astrophysics research. The SPH method has been gradually applied to studying hydrodynamics and has shown significant advantages. Monaghan [8] was the first to apply the SPH method to solve a fluid dynamics problem, and since then, the method has been rapidly developed and applied. Additionally, the increase in the use of the SPH method has motivated the development of other hydrodynamic methods and theories.

Jiang et al. [9] studied the liquid-sloshing characteristics of an elastic rectangular tank at different horizontal excitation frequencies and obtained the free-surface height and pressure change curves of the tank. Liu et al. [10] improved the SPH method to numerically simulate the liquid sloshing in a rhombus liquid tank at different filling depths, external frequencies, and amplitudes and analyzed strong nonlinear phenomena such as rolling and breaking. Huang et al. [11] studied the feasibility of implementing an SPH algorithm to analyze liquid sloshing and the effects of liquid volume, sloshing angle, liquid material property, and cycle. Additionally, the filling depth of the liquid tank under the maximum impact load was obtained. Hao et al. [12] used the SPH method to simulate the sloshing of the fuel in a missile tank under pitch and roll excitation. Furthermore, the impact force and impact torque produced by the sloshing liquid were determined, and the effects of the change law of the center of gravity of the liquid on the stability of the missile were examined. Cardoso-Ribeiro et al. [13] proposed port-Hamiltonian systems (PHs) for formulating the liquid-sloshing equations of moving containers and beam structural equations using piezoelectric actuators. The PH model proved useful for designing an active control law for the reducing the sloshing phenomenon. Hasheminejad and Soleimani [14] investigated using modified cylindrical Bessel functions the free three-dimensional (3D) sloshing in a finite-span circular cylindrical vessel that was partially filled, rigid-walled, and horizontally mounted. The numerical simulations illustrated the important effects of the container length and depth of the filled liquid on the calculated sloshing frequencies. Nicolsen et al. [15] developed a new total Lagrangian continuum-based liquid-sloshing model for a vehicle. The results demonstrated that liquid sloshing changed the contact forces between the tires and ground and thereby increased the forces on certain wheels while decreasing the forces on the other wheels. Farid and Gendelman [16] developed an equivalent mechanical model of the nonlinear liquid sloshing occurring in a partially liquid-filled vessel and explored its dynamic regimes. All the analytical predictions were in good agreement with the direct numerical simulations of the initial reduced-order model.

The aforementioned research mainly introduced and solved the sloshing caused by a liquid-carrying storage tank on the surface of the earth. For aerospace field applications, the effect of sloshing on a vehicle and the attitude accuracy must be considered. If the amplitude of the liquid sloshing in a spacecraft increases, then its attitude angle will also increase under the sloshing inertia force, which will diverge the spacecraft attitude movement. Liquid sloshing will also cause a change in the liquid centroid, which will produce a change in the attitude angle. Concurrently, the change in the attitude angle will further aggravate the liquid sloshing. This coupled effect will destabilize the spacecraft centroid and affect the attitude control. Because of these challenges, the study of liquid sloshing is gaining attention of aerospace researchers.

Considering the large amplitude of the liquid sloshing occurring in a spacecraft storage tank, Hang et al. [17] established a 3D surface-equivalent model of the centroid moving arbitrarily. The simulation results were compared with the numerical results based on the volume-of-fluid method to verify the effectiveness of the model for the analysis of liquid sloshing. Ahmad and Yue [18] developed a canonical liquid-sloshing Hamiltonian model for a container coupled with a spacecraft. The results demonstrated that the Hamiltonian–Casimir technique was effective for studying the spacecraft attitude dynamics, aerodynamics, and other fluid-carrying moving bodies that could be affected by liquid sloshing. Lazzarin et al. [19] studied the impact of propellant sloshing on the pointing stability of the EUCLID satellite. A new method was proposed and applied to a specific fluid system based on computational fluid dynamics instead of real experiments. Zhou and Huang [20] developed a 3D constraint surface mechanical model for the large-amplitude sloshing in propellant tanks. The

model validation was further extended to include the in-orbit experimental data of the SloshSat FLEVO satellite, and the numerical results agreed with the experimental data. Chiba and Magata [21] studied the effect of liquid sloshing on the dynamics of flexible space structures. The results indicated that the vibration characteristics of the coupled system were dependent on the static contact angle of the liquid. Although these studies were aimed at the liquid-sloshing characteristics of spacecrafts and their effect on the structure and attitude of the orbiting spacecrafts, they did not provide a method for effectively establishing the relationship between the angular velocity of the satellite attitude and various disturbance factors.

Herein, to determine the effect of liquid sloshing on the satellite attitude angular velocity and accuracy of the satellite attitude control during orbit, a method for predicting the liquid-sloshing characteristics of a microsatellite propulsion system is proposed. Three states are considered for the following models for determining the liquid-sloshing characteristics: (1) storage tank, (2) coupling of the storage tank and microsatellite, and (3) coupling of the storage tank and microsatellite with a deployment mechanism. The SPH method is used to study the effect of the sloshing on the storage tank and microsatellite disturbance for each of the three states. The relationship models between the sloshing time, sloshing angular velocity, amount of fluid filled, and satellite attitude angular velocity are established. The models are then used to predict the disturbance angular velocity of the microsatellite, which is compared with the orbital satellite data to illustrate the accuracy of the analysis and model. The results of this study can provide theoretical guidance for the engineering design and orbit control of a microsatellite propulsion system.

2. Liquid-Ammonia Propulsion System of a Microsatellite

The liquid-ammonia propulsion system of a microsatellite considered here as reference mainly consists of a storage tank, pipeline, filter, pressure sensor, injection port, isolation valve, battery valve, and thruster, as shown in Figure 1. Because of the envelope-size limitation, the storage tank design is approximated as a column structure with an elliptical cross section. The storage tank has a height, width, length, and thickness of 66 mm, 130 mm, 112 mm, and 2.1 mm, respectively. The tank quality is 0.368 kg and the volume is 0.607 L. The ammonia propellant fills the inside of the storage tank under a pressure of 2.4 MPa, and it can be liquefied.

As previously mentioned, the following three models are established to analyze the effect of the propellant-filled storage tank on the attitude angular velocity of the storage tank and satellite: (1) storage tank model, (2) storage tank and microsatellite coupling model, and (3) storage tank and microsatellite with a deployment mechanism coupling model. The satellite has a 250 mm^3 volume with a mass of 20 kg. The deployment mechanism is a hexagonal structure with a mass of 5 kg. Based on the installation of the microsatellite propulsion system, the storage tank propulsion system

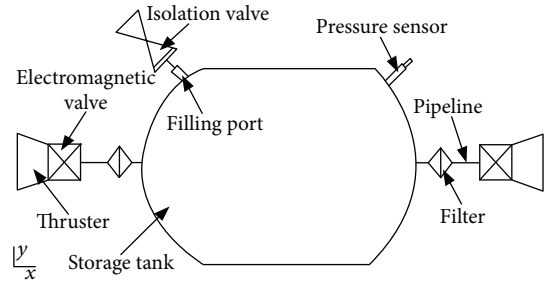

Figure 1: Propulsion system composition.

is connected to the satellite by a fixture tool, and the center of the storage tank coincides with the geometric center of the satellite. The geometry of the storage tank and a simplified illustration of its installation on the satellite are shown in Figure 2, and the moments of inertia of the three models when the storage tank is filled with a propellant are presented in Table 1.

3. SPH Theory

The SPH method uses a series of randomly distributed disconnected particles to represent the problem domain. The integral method is used to approximate the field function. Furthermore, the particles are used to approximate the kernel equation. The sum of the superposition values of the adjacent particles in a local region is used to replace the integral of the field function and its derivative. The particle-approximation process is conducted at each time step, and therefore, the number of particles used depends on the current locally distributed particles. The particle approximation method is applied to all field functions, and a series of process quantities that are discretized with time are obtained. The process quantities are solved by the explicit integration method to obtain the fastest time integral.

3.1. Basic Principle of the SPH. The kernel approximation method is the gradual integration of any function with a smooth function. The integral form of any continuous function in variable field Ω can be expressed as

$$f(x) = \int_{\Omega} f\left(x'\right)\delta\left(x - x'\right)\mathrm{d}x', \tag{1}$$

where $f(x)$ is a continuous function of coordinate vector x in variable field Ω, which is the integral volume including vectors x. $\delta(x - x')$ is the Dirac δ function, which can be expressed as

$$\delta\left(x - x'\right) = \begin{cases} 1, & x = x', \\ 0, & x \neq x'. \end{cases} \tag{2}$$

Next, $\delta(x - x')$ is replaced with $W(x - x', h)$, which has features similar to δ. In the SPH method, the angle brackets

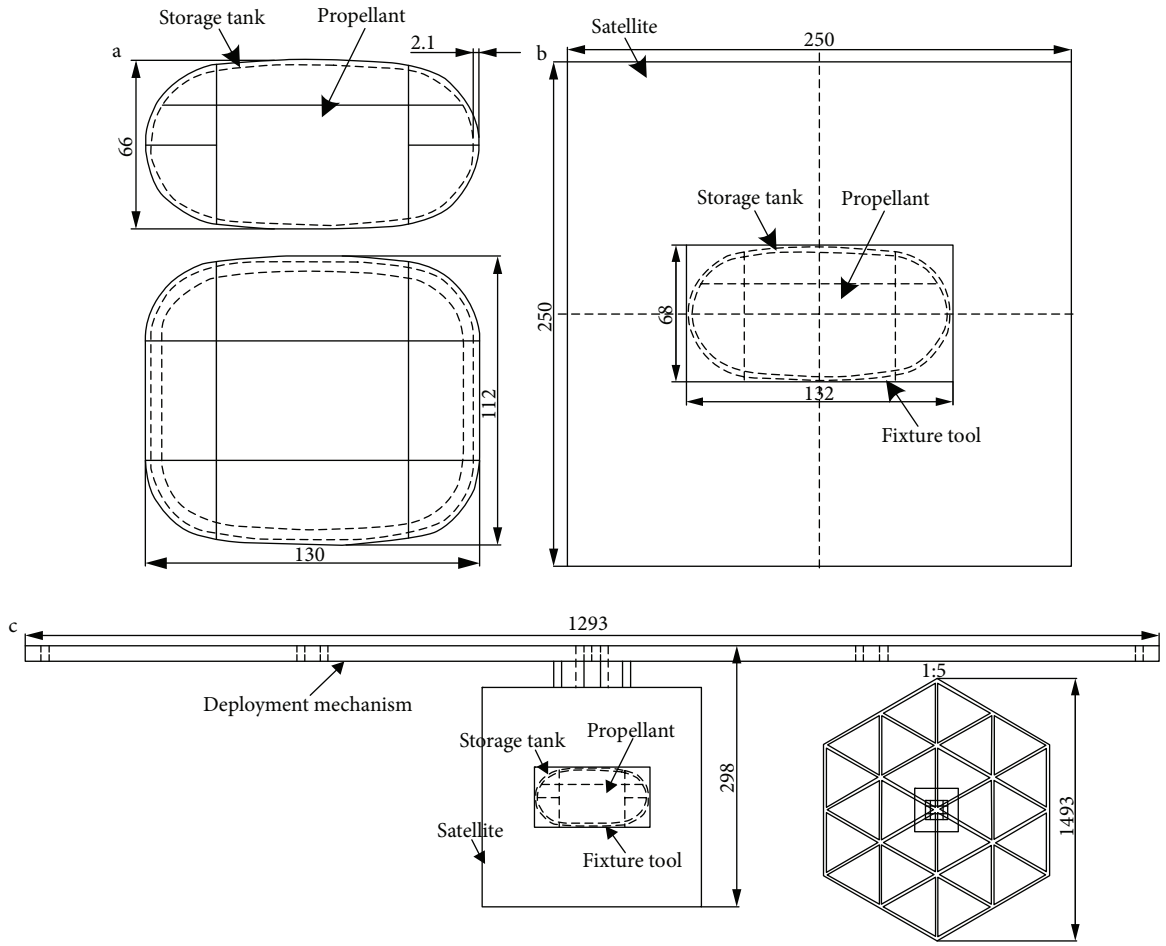

Figure 2: The shape and size of the storage tank and the position of the installation in the satellite: (a) the storage tank model; (b) the storage tank and microsatellite coupling model; (c) the storage tank and microsatellite with a deployment mechanism coupling model.

Table 1: The moment of inertia of three cases.

Case	Weight (kg)	I_{xx} (kg m^2)	I_{yy} (kg m^2)	I_{zz} (kg m^2)
1	0.632	1.111×10^{-3}	0.892×10^{-4}	1.456×10^{-3}
2	15.234	0.161	0.168	0.155
3	20	0.933	0.936	1.501

mark the kernel-approximation function, and the integral can be written in the following form:

$$\langle f(x)\rangle = \int_{\Omega} f\left(x'\right) W\left(x - x', h\right) \mathrm{d}x', \tag{3}$$

where $W(x - x', h)$ is the smoothing kernel function and h is the smoothing length, which is the distance between particles x and x' and governs the size of the support domain of the kernel function.

If the density of particle j is ρ_j, for $j = 1, 2, \ldots, N$, the mass is m_j, and N is the total number of particles present in the particle support domain, then the particle approximation function of particle i can be obtained by the discretization of (3).

$$\langle f(x_i)\rangle = \sum_{j=1}^{N} \frac{m_j}{\rho_j} f\left(x_j\right) W_{ij}\left(x - x', h\right). \tag{4}$$

By using the differentiability of the kernel function, the particle approximation of the function-space derivative is derived as follows:

$$\langle \nabla f(x_i)\rangle = \sum_{j=1}^{N} \frac{m_j}{\rho_j} f\left(x_j\right) \nabla W_{ij}\left(x - x', h\right). \tag{5}$$

Equations (4) and (5) show that the particle-approximation equation converts the continuous integral expression of the function and derivative into a discrete sum of arbitrarily arranged particles, thereby realizing a mesh-less space.

A commonly used kernel function is a piecewise third-order function that was proposed by Monaghan.

$$W(R,h) = a_{\mathrm{d}} \begin{cases} \frac{2}{3} - R^2 + \frac{1}{2}R^3, & 0 \le R < 1, \\ \frac{1}{6}(2-R)^3, & 1 \le R \le 2, \\ 0, & R > 2, \end{cases} \tag{6}$$

where R is the relative distance between particles x and x' and a_{d} is $1/h$, $15/7\pi h^2$, and $3/2\pi h^3$ in the one-dimensional, two--dimensional, and 3D space, respectively.

The mass, momentum, and energy conservation equations for continuum fluid dynamics are as follows:

$$\frac{\mathrm{d}\rho}{\mathrm{d}t} = -\rho \nabla U, \tag{7}$$

$$\frac{\mathrm{d}U}{\mathrm{d}t} = -\rho \nabla \sigma, \tag{8}$$

$$\frac{\mathrm{d}E}{\mathrm{d}t} = -\frac{P}{\rho} \nabla U, \tag{9}$$

where ρ is the fluid density, U is the velocity vector, σ is the stress tensor, E is the energy, P is hydrostatic pressure, and t is the time.

By the transformation of (7)–(9), the following equations are obtained:

$$\frac{\mathrm{d}\rho_i}{\mathrm{d}t} = -\sum_{j=1}^{N} m_j (u_i - u_j) \nabla W_{ij}, \tag{10}$$

$$\frac{\mathrm{d}u_i}{\mathrm{d}t} = -\sum_{j=1}^{N} m_j \left(\frac{\sigma_i}{\rho_i} - \frac{\sigma_j}{\rho_j} \right) \nabla W_{ij}, \tag{11}$$

$$\frac{\mathrm{d}E_i}{\mathrm{d}t} = \sum_{j=1}^{N} \frac{m_j (P_i + P_j)}{2\rho_i \rho_j} (U_i - U_j) \nabla W_{ij}, \tag{12}$$

where $W_{ij} = W(x_i - x_j, h)$ and $\mathrm{d}\rho_i/\mathrm{d}t$, $\mathrm{d}U_i/\mathrm{d}t$, and $\mathrm{d}E_i/\mathrm{d}t$ represent the derivative of the corresponding physical quantity of particle i.

3.2. Calculation Process of the SPH Finite-Element Method. The SPH finite-element particle method expresses the spatial derivative of a function as an algebraic equation of particle summation, but a physical quantity is a continuous function of time. First, the continuum is discretized into a series of SPH particles having a mass. The velocity of the particles is obtained using the momentum conservation equation, and the space coordinates of the particles are calculated. Next, the strain rates are obtained using the geometric relations, and then the density of the particles is obtained from the mass conservation equation. Then, the specific internal energy of the particles is obtained using the energy equation. The hydrostatic pressure and stress tensor are calculated by applying the state equation, and the calculated data are stored. A loop calculation is performed until the end of the analysis step. The calculation process of the SPH finite-element method is displayed in Figure 3.

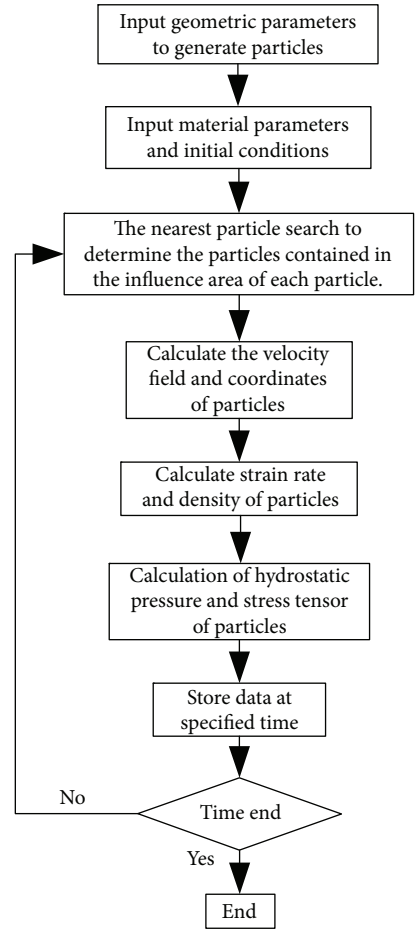

Figure 3: The calculation process of the SPH finite element method.

4. Analysis of the Initial Liquid Sloshing in the Storage Tank

The attitude and orbit adjustment of a satellite will cause sloshing of a liquid-filled storage tank, leading to satellite disturbance, which will further affect the attitude and orbit control precision. The disturbance produced by excessive liquid sloshing will increase the difficulty of attitude control. To further clarify the effect of the storage tank sloshing on satellite attitude angular velocity, it is necessary to analyze the liquid sloshing of the storage tank under different working conditions. This analysis will assist in determining the effect of liquid sloshing on satellite attitude angular velocity and improve the accuracy of satellite attitude control during orbit.

To analyze the attitude disturbance produced by the three different states of storage tank sloshing, the three models are rotated around the orthogonal-body-fixed reference-frame axes. Furthermore, when the storage tank-filled propellant is in orbit, the propellant distribution in the storage tank is different from that when it is on ground. To ignore the

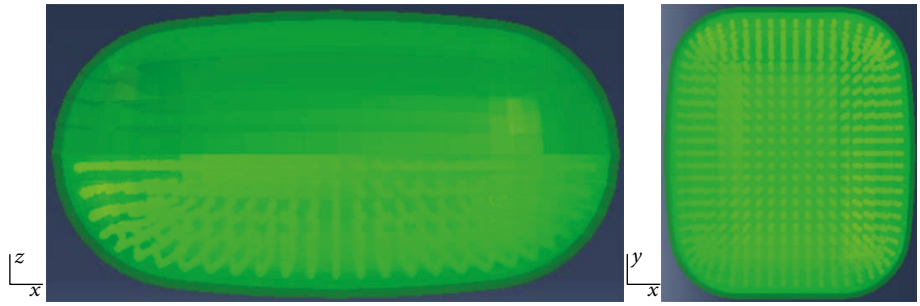

Figure 4: The finite element analysis model of the storage tank.

Table 2: The material properties for the storage tank.

Material	Density (kg/m^3)	Modulus of elasticity (GPa)	Poisson ratio	Yield strength (MPa)	Tensile strength (MPa)
TC4	4500	120	0.3	850	1100

difference and for research convenience, we assume that the distribution of the propellant in the storage tank is same as that on the ground. This simplifies the boundary conditions of the contact between the storage tank and propellant. The inside of the storage tank is assumed to be pure liquid ammonia, and the state of the gas–liquid two-phase mixture is not considered. Additionally, the effects of gravity are not considered. A finite-element analysis model of the storage tank for different amounts of fluid fill is established, as presented in Figure 4. The material of the storage tank is TC4, and the material properties are listed in Table 2. The tank is divided into 2384 elements and 3606 nodes by the C3D8R mesh type. For the SPH model, the liquid C3D8R solid element is converted to the PC3D particle element. The grid of the elements is 6 mm, the storage tank motion is coupled to the geometric center of storage tank, and a general contact is defined. Because the inner surface of the storage tank is rough, the friction formulation between the tank and liquid ammonia is of rough type. Double-precision analysis is applied in the ABAQUS finite-element software.

The behavior of liquid materials during sloshing is very complex. It is necessary to use the equations of state to describe the pressure, volume, and energy characteristics of the materials. The isotropic pressure can be obtained from the Mie–Gruneisen equation of state,

$$P(\rho, e) = \left(1 - \frac{1}{2}\Gamma_0\eta\right)P_H + \Gamma_0\rho_0 E_{\mathrm{m}}, \tag{13}$$

$$P_H = \frac{\rho_0 c^2 \eta}{(1 - s\eta)^2}, \tag{14}$$

where H is the Hugoniot curve, E_{m} is the internal energy of the unit mass, $\eta = (\rho/\rho_0) - 1$ is the nominal volume-compression rate, Γ_0 is the Gruneisen constant, s is the limit volume-compression rate, and c is the sound velocity in liquid ammonia. When the nominal strain is small, the volume modulus is $K = \rho_0 c^2$. c and s can be described by a linear relation between the shock velocity and particle velocity.

$$U_{\mathrm{s}} = c + sU_{\mathrm{p}}, \tag{15}$$

where U_{s}-U_{p}, the Hugoniot equation of state, provides a moving-liquid material model in which the volume strength of the material is determined. The storage tank propellant is liquid ammonia, whose performance parameters are listed in Table 3.

The rotation or disturbance of a storage tank during orbit is mainly caused by the angular velocity produced by the satellite attitude control and satellite separation from the rocket. Hence, the geometric center of the storage tank is assumed as the coordinate origin, the angular velocity is applied around the XYZ axes, and the angular velocity of the rotation process is as follows:

$$\omega_i = \begin{cases} \omega_{i_0} t, & 0 \le t \le 1, \\ \omega_{i_0} & 0 \le t \le 1, \end{cases} \tag{16}$$

where $i = x, y, z$ and ω_{i_0} is the initial angular velocity.

To obtain an accurate disturbance angular velocity, the stable angular velocity is represented by the mean value of the disturbance angular velocity, which can be expressed as

$$\omega_i' = \begin{cases} 0, & 0 \le t \le t_i - 1, \\ \sum_{j=1}^{k} \dfrac{\omega_j'}{k}, & t > t_i - 1, \end{cases} \tag{17}$$

where ω_i' is the mean value of the disturbance angular velocity, ω_j' is the output value of the disturbance angular velocity, k is the number of output values, and t_i is the total time when $i = x, y, z$.

The following two states are analyzed with a sloshing angular velocity of 10°/s and rotation time of 5 s: (1) empty storage tank and (2) liquid storage tank that is 50% full. Once the angular velocity is applied, the rotation constraint is removed. The angular velocity of the storage tank throughout the process is analyzed, and the analysis results are presented in Figures 5 and 6 and Table 4.

Figures 5 and 6 and Table 4 demonstrate that the liquid in the storage tank affects the disturbance angular velocity,

Table 3: The performance parameters of the liquid ammonia.

TC4	Density (kg/m^3)	The speed of sound (m/s)	Viscosity (kg/m s)	Coefficient of state equation	
				s	Γ_0
Liquid ammonia	729	1100	2.55×10^{-4}	0	0

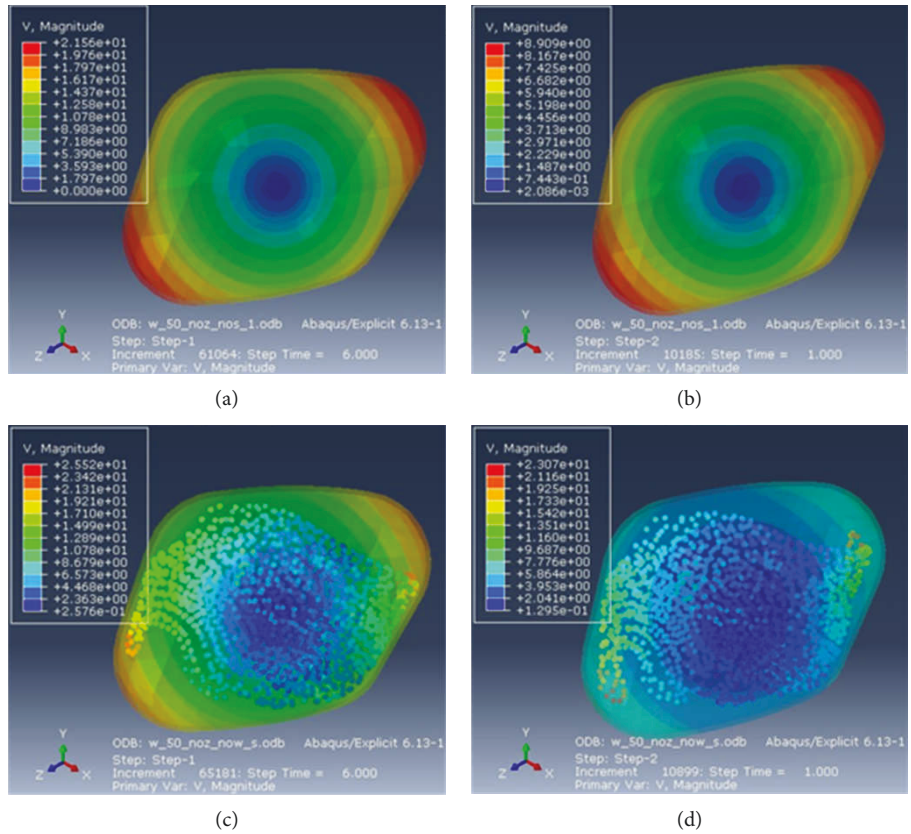

Figure 5: Moving speed of the storage tank and liquid: (a) the empty storage tank after 6 s; (b) the empty storage tank after 7 s; (c) the liquid storage tank after 6 s; (d) the liquid storage tank after 7 s.

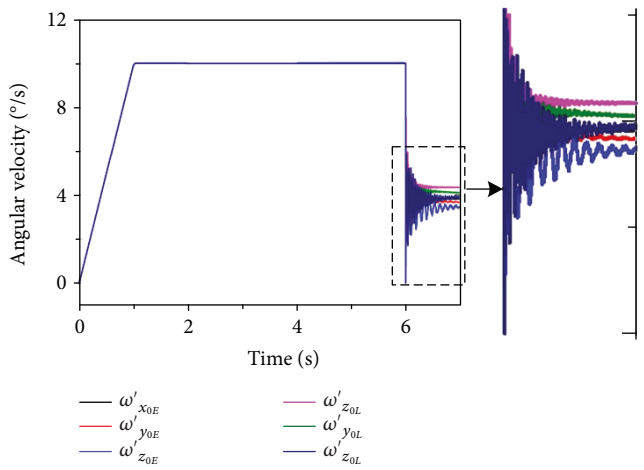

Figure 6: The disturbance angular velocity.

which after the filling of the storage tank is higher than that of the empty storage tank. The fluid flow increases the disturbance angular velocity of the storage tank owing to the angular velocity of the storage tank rotation. Table 4 shows that the disturbance angular velocity is directly determined by the sloshing time, sloshing angular velocity, and amount of the fluid filled. The disturbance angular velocity directly governs the attitude-control precision of the satellite. Hence, further optimization and analysis are required to determine the effect of the satellite rotation angle, causing propellant sloshing, on the satellite attitude.

5. Sloshing Analysis

Owing to the limited energy available on a microsatellite, the attitude-control ability is poor. An attitude-control subsystem imposes corresponding requirements on the initial attitude after separation from the rocket to place the satellite in orbit. The detailed requirements are listed in Table 5.

Table 4: Simulation results of the empty storage tank and liquid storage tank.

Status	t (s)	ω_x (°/s)	ω_y (°/s)	ω_z (°/s)	ν (%)	ω'_{x_0} (°/s)	ω'_{y_0} (°/s)	ω'_{z_0} (°/s)
Empty storage tank	5	10	10	10	0	3.495	3.69	3.428
Liquid storage tank	5	10	10	10	50	4.342	4.096	3.903

Table 5: Technical indices of attitude angular velocity for microsatellite.

No.	Technical specification	Design value
1	Rolling angular velocity/(°/s)	$\lvert\Delta\omega_\gamma\rvert \le 2$
2	Pitch velocity/(°/s)	$\lvert\Delta\omega_\phi\rvert \le 3$
3	Yaw velocity/(°/s)	$\lvert\Delta\omega_\varphi\rvert \le 3$

Table 6: Parameter-level table.

Level	t (s)	ω_x (°/s)	ω_y (°/s)	ω_z (°/s)	ν (%)
1	1	2	2	2	10
2	2	4	4	4	20
3	3	6	6	6	30
4	4	8	8	8	40
5	5	10	10	10	50
6	6	12	12	12	60
7	7	14	14	14	70
8	8	16	16	16	80
9	10	18	18	18	90
10	12	20	20	20	100

Table 7: Five factors and ten levels uniform test table.

Level	t (s)	ω_x (°/s)	ω_y (°/s)	ω_z (°/s)	ν (%)
1	5	16	4	16	90
2	6	2	12	14	10
3	10	10	14	12	100
4	3	12	6	4	20
5	4	4	20	6	80
6	1	18	16	10	40
7	2	8	8	20	60
8	8	14	18	18	30
9	9	6	2	8	50
10	7	20	10	2	70

To determine the law of the liquid sloshing in the storage tank, several simulation analyses of the storage tank under different states are discussed below.

5.1. Sloshing Analysis of the Storage Tank. To study the disturbance angular velocity of the liquid-sloshing process of the storage tank at different sloshing times, sloshing angular velocities, and liquid-fill volumes, the sloshing time range, sloshing angular velocity, and amount of the filled liquid

Table 8: Simulation results of empty storage tank.

No.	t (s)	ω_x (°/s)	ω_y (°/s)	ω_z (°/s)	ω'_{x_1} (°/s)	ω'_{y_1} (°/s)	ω'_{z_1} (°/s)	Computation time in ABAQUS (s)
1	5	16	4	16	6.458	1.999	5.174	147
2	6	2	12	14	0.807	4.245	4.707	166
3	10	10	14	12	4.021	5.215	4.328	218
4	3	12	6	4	4.887	2.275	1.289	117
5	4	4	20	6	2.011	6.653	1.563	133
6	1	18	16	10	6.356	5.678	3.101	99
7	2	8	8	20	3.015	2.411	6.391	106
8	8	14	18	18	5.125	6.456	5.717	186
9	9	6	2	8	2.189	0.939	2.561	216
10	7	20	10	2	6.894	3.988	0.715	189

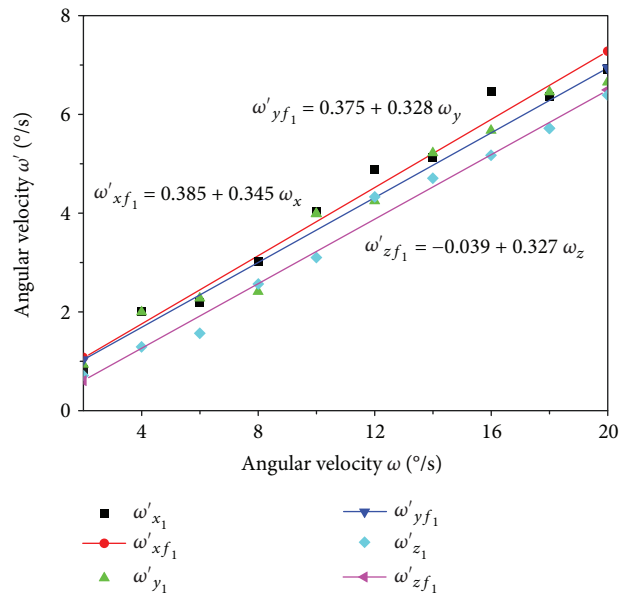

Figure 7: Fitting polynomial and fitting results of empty storage tank for ω'_{xf_1}, ω'_{yf_1}, and ω'_{zf_1}.

Table 9: ω'_{xf_1}, ω'_{yf_1}, and ω'_{zf_1} of the linear regression equations.

No.	Regression equation	Multiple R
1	$\omega'_{xf_1} = 0.385 + 0.345\omega_x$	0.988
2	$\omega'_{yf_1} = 0.375 + 0.328\omega_y$	0.99
3	$\omega'_{zf_1} = -0.039 + 0.327\omega_z$	0.994

Table 10: Simulation results of liquid storage tank.

No.	t (s)	ω_x (°/s)	ω_y (°/s)	ω_z (°/s)	ν (%)	ω'_{x_2} (°/s)	ω'_{y_2} (°/s)	ω'_{z_2} (°/s)	Computation time in ABAQUS (s)
1	5	16	4	16	90	7.519	2.401	7.037	1346
2	6	2	12	14	10	0.938	4.774	6.038	432
3	10	10	14	12	100	4.765	6.058	5.876	2580
4	3	12	6	4	20	5.568	2.587	1.744	323
5	4	4	20	6	80	2.366	7.722	2.521	1172
6	1	18	16	10	40	7.367	6.477	4.299	377
7	2	8	8	20	60	3.582	2.926	8.476	723
8	8	14	18	18	30	5.936	7.291	7.482	838
9	9	6	2	8	50	2.644	1.162	3.549	1330
10	7	20	10	2	70	8.135	4.596	1.238	1570

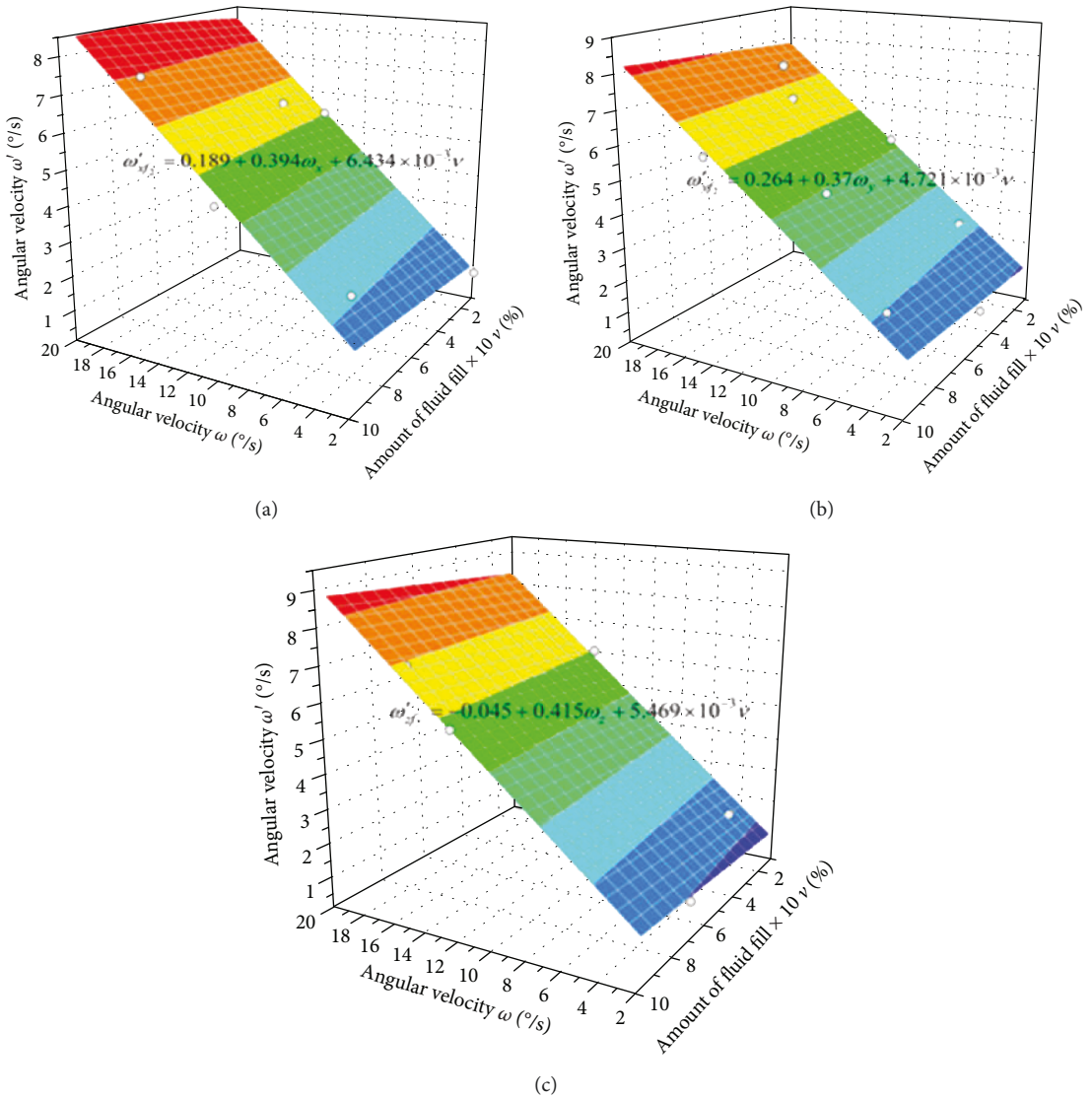

Figure 8: Fitting polynomial and surface fitting results of liquid storage tank for (a) ω'_{xf_2}, (b) ω'_{yf_2}, and (c) ω'_{zf_2}.

are limited to 1–12 s, 2–20°/s, and 10–100%, respectively, based on the actual situation of such a satellite in orbit. Table 6 presents the factor parameter levels without considering the mixing of the parameters. A uniform test table containing five factors and ten levels is established and summarized in Table 7. Ten storage tank models are

Table 11: ω'_{xf_2}, ω'_{yf_2}, and ω'_{zf_2} of the surface regression equations.

No.	Regression equation	Multiple R
1	$\omega'_{xf_2} = 0.189 + 0.394\omega_x + 6.434 \times 10^{-3}\nu$	0.993
2	$\omega'_{yf_2} = 0.264 + 0.37\omega_y + 4.721 \times 10^{-3}\nu$	0.992
3	$\omega'_{zf_2} = -0.045 + 0.415\omega_z + 5.469 \times 10^{-3}\nu$	0.997

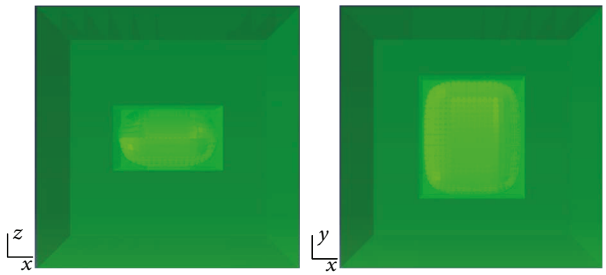

Figure 9: Finite element analysis model that couples the storage tank and microsatellite.

Table 12: Material characteristics for the microsatellite.

Material	Density (kg/m^3)	Modulus of elasticity (GPa)	Poisson ratio	Yield strength (MPa)	Tensile strength (MPa)
2A12	2780	72	0.3	270	440

Table 13: Simulation results of empty storage tank and microsatellite.

No.	t (s)	ω_x (°/s)	ω_y (°/s)	ω_z (°/s)	ω'_{x_3} (°/s)	ω'_{y_3} (°/s)	ω'_{z_3} (°/s)	Computation time in ABAQUS (s)
1	5	16	4	16	7.97	1.963	8.108	238
2	6	2	12	14	0.799	6.163	7.462	248
3	10	10	14	12	5.478	7.036	6.264	347
4	3	12	6	4	6.063	3.176	2.11	181
5	4	4	20	6	1.934	10.699	3.305	196
6	1	18	16	10	8.976	8.481	5.196	131
7	2	8	8	20	3.801	4.206	10.137	156
8	8	14	18	18	7.7	9.287	9.232	303
9	9	6	2	8	2.951	1.002	4.069	317
10	7	20	10	2	10.436	4.868	1.068	259

established and input to the ABAQUS software for the simulation analysis, and the final results and computation time are summarized in Table 8. The fitting results of the linear regression analysis are shown in Figure 7, and the values of ω'_{xf_1}, ω'_{yf_1}, and ω'_{zf_1} from the linear regression equations are presented in Table 9.

To further analyze the disturbance angular velocity of the liquid sloshing of the storage tank under different sloshing times, sloshing angular velocities, and liquid-fill volumes,

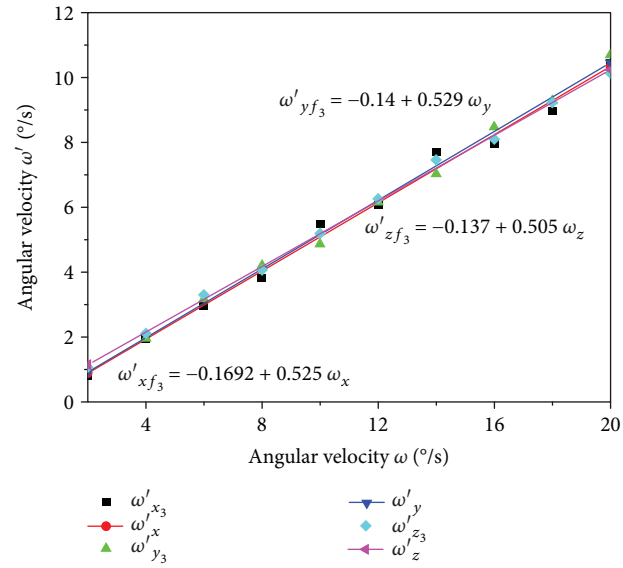

Figure 10: Fitting polynomial and fitting results of empty storage tank and microsatellite for ω'_{xf_3}, ω'_{yf_3}, and ω'_{zf_3}.

Table 14: ω'_{xf_3}, ω'_{yf_3}, and ω'_{zf_3} of the linear regression equations.

No.	Regression equation	Multiple R
1	$\omega'_{xf_3} = -0.169 + 0.525\omega_x$	0.996
2	$\omega'_{yf_3} = -0.14 + 0.529\omega_y$	0.999
3	$\omega'_{zf_3} = 0.137 + 0.505\omega_z$	0.999

similar to the previous analyses, which did not consider the mixing among the various factors, the sloshing time range of the tank, sloshing angular velocity, and amount of the filled liquid in the storage tank are limited to 1–12 s, 2–20°/s, and 10–100%, respectively. Additionally, a uniform test table of five factors and ten levels is generated, and ten storage tank models are established and analyzed by ABAQUS. The final simulation analysis results and computation time are listed in Table 10, fitting results are shown in Figure 8, and values of ω'_{xf_2}, ω'_{yf_2}, and ω'_{zf_2} from the surface regression equations are presented in Table 11.

5.2. Sloshing Analysis of the Storage Tank in Microsatellite. The analysis results in Sloshing Analysis of Storage Tank indicate that it is necessary to analyze the sloshing by coupling the storage tank and microsatellite to evaluate the effect of the sloshing on the satellite attitude angular velocity. Accordingly, a finite-element analysis model that couples the storage tank and microsatellite with different amounts of the filled liquid is established, as shown in Figure 9. The parameters of the microsatellite materials are listed in Table 12. The size of the storage tank, grid divisions, and performance of the liquid material are the same as those in Section 5.1. The satellite is divided into 1408 elements and 1014 nodes using the C3D8R mesh type.

Table 15: Simulation results of liquid storage tank and microsatellite.

No.	t (s)	ω_x (°/s)	ω_y (°/s)	ω_z (°/s)	ν (%)	ω'_{x_4} (°/s)	ω'_{y_4} (°/s)	ω'_{z_4} (°/s)	Computation time in ABAQUS (s)
1	5	16	4	16	90	8.203	2.088	8.273	1402
2	6	2	12	14	10	0.828	6.252	7.548	514
3	10	10	14	12	100	5.644	7.227	6.416	3000
4	3	12	6	4	20	6.216	3.231	2.149	354
5	4	4	20	6	80	2.009	10.897	3.406	1224
6	1	18	16	10	40	9.195	8.616	5.287	360
7	2	8	8	20	60	3.928	4.307	10.298	772
8	8	14	18	18	30	7.868	9.431	9.357	882
9	9	6	2	8	50	3.049	1.073	4.156	1422
10	7	20	10	2	70	10.729	5.004	1.139	1615

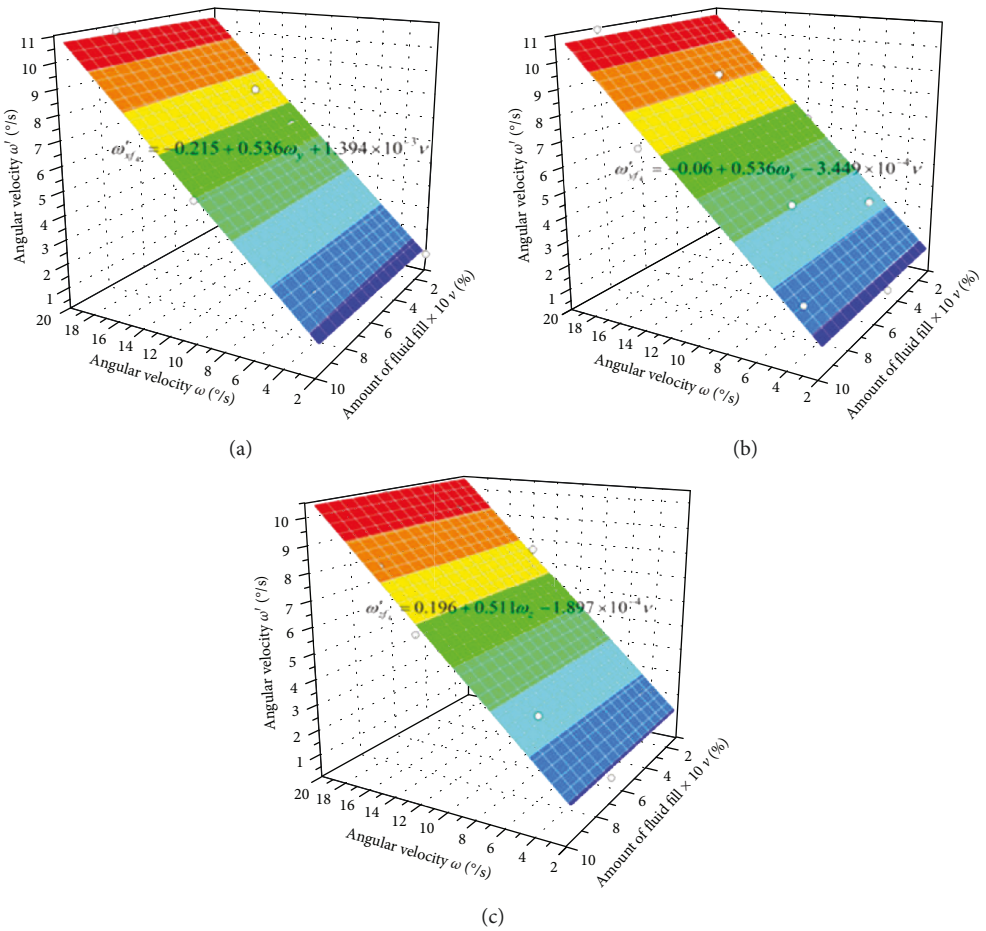

Figure 11: Fitting polynomial and surface fitting results of liquid storage tank and microsatellite for (a) ω'_{xf_4}, (b) ω'_{yf_4}, (c) ω'_{zf_4}.

Using the sloshing times, sloshing angular velocity, and amounts of filled liquid in the storage tank that are presented in Section 5.1, a uniform test table is established containing four factors and ten levels. The final simulation analysis results and computation time obtained using ABAQUS are presented in Table 13, fitting results are shown in Figure 10, and values of ω'_{xf_3}, ω'_{yf_3}, and ω'_{zf_3} from the linear regression equations are listed in Table 14.

Table 16: ω'_{xf_4}, ω'_{yf_4}, and ω'_{zf_4} of the surface regression equations.

No.	Regression equation	Multiple R
1	$\omega'_{xf_4} = -0.215 + 0.536\omega_x + 1.394 \times 10^{-3}\nu$	0.997
2	$\omega'_{yf_4} = -0.06 + 0.536\omega_y - 3.449 \times 10^{-4}\nu$	0.999
3	$\omega'_{zf_4} = 0.196 + 0.511\omega_z - 1.897 \times 10^{-4}\nu$	0.999

Figure 12: Finite element model of storage tank and microsatellite with the deployment mechanism.

Table 17: Material parameters of the deployment mechanism.

Material	Density (kg/m^3)	Modulus of elasticity (GPa)	Poisson ratio	Tensile strength (MPa)
Carbon fiber T700	1800	126	0.31	3500

Table 18: Simulation results of empty storage tank and microsatellite with the deployment mechanism.

No.	t (s)	ω_x (°/s)	ω_y (°/s)	ω_z (°/s)	ω'_{x_5} (°/s)	ω'_{y_5} (°/s)	ω'_{z_5} (°/s)	Computation time in ABAQUS (s)
1	5	16	4	16	2.596	0.677	1.826	1065
2	6	2	12	14	0.368	1.813	1.518	1247
3	10	10	14	12	1.489	2.212	1.231	1904
4	3	12	6	4	1.762	0.962	0.38	781
5	4	4	20	6	0.512	3.081	0.558	969
6	1	18	16	10	2.858	2.541	0.972	502
7	2	8	8	20	1.112	1.232	2.234	650
8	8	14	18	18	2.166	2.868	2.076	1548
9	9	6	2	8	0.809	0.345	0.774	1690
10	7	20	10	2	3.133	1.521	0.271	1429

The coupled sloshing of the propellant and microsatellite is concurrently analyzed. The final simulation results and computation time obtained from ABAQUS are listed in Table 15, fitting results are shown in Figure 11, and values of ω'_{xf_4}, ω'_{yf_4}, and ω'_{zf_4} of the surface regression equations are provided in Table 16.

5.3. Analysis of the Storage Tank and Microsatellite with the Deployment Mechanism. Based on the analysis results of Sections 5.1 and 5.2, the disturbance angular velocity of the storage tank varies in different states. The satellite has an unfolding mechanism for use during orbit. Therefore, it is necessary to analyze the effect of the sloshing in the storage tank and microsatellite with the deployment mechanism on the satellite attitude angular velocity. A finite-element analysis model with different filled liquid levels in the storage tank and microsatellite with the deployment mechanism is established, as shown in Figure 12. The material parameters of the deployment mechanism are listed in Table 17. The deployment mechanism is divided into 344 elements and 1218 nodes using the C3D8R mesh type. A test table of four factors and ten levels is established to obtain the simulation results and computation time in ABAQUS, as presented in Table 18. The fitting results are displayed in Figure 13, and the values of ω'_{xf_5}, ω'_{yf_5}, and ω'_{zf_5} from the linear regression equations are listed in Table 19.

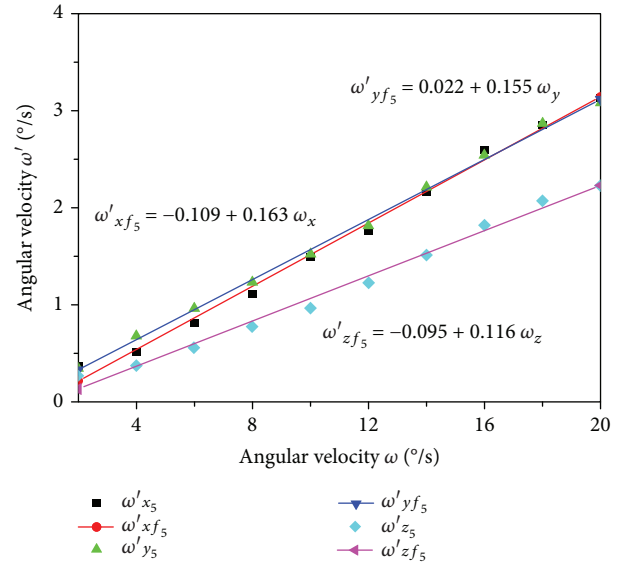

Figure 13: Fitting polynomial and fitting results of empty storage tank and microsatellite with the deployment mechanism for ω'_{xf_5}, ω'_{yf_5}, and ω'_{zf_5}.

Table 19: ω'_{xf_5}, ω'_{yf_5}, and ω'_{zf_5} of the linear regression equations.

No.	Regression equation	Multiple R
1	$\omega'_{xf_5} = -0.109 + 0.163\omega_x$	0.997
2	$\omega'_{yf_5} = 0.022 + 0.155\omega_y$	0.999
3	$\omega'_{zf_5} = -0.095 + 0.116\omega_z$	0.995

The sloshing in the liquid storage tank and microsatellite with the deployment mechanism is analyzed similarly. The results of the final simulation analysis and computation time obtained from ABAQUS are given in Table 20, fitting results are shown in Figure 14, and values of ω'_{xf_6}, ω'_{yf_6}, and ω'_{zf_6} from the surface regression equations are presented in Table 21.

5.4. Analysis of the Sloshing Characteristics and Comparison of the Calculation and Simulation. The above analysis demonstrated a linear relationship between the disturbance

Table 20: Simulation results of liquid storage tank and microsatellite with the deployment mechanism.

No.	t (s)	ω_x (°/s)	ω_y (°/s)	ω_z (°/s)	ν (%)	ω'_{x_6} (°/s)	ω'_{y_6} (°/s)	ω'_{z_6} (°/s)	Computation time in ABAQUS (s)
1	5	16	4	16	90	2.649	0.716	1.883	6993
2	6	2	12	14	10	0.375	1.839	1.547	2696
3	10	10	14	12	100	1.536	2.273	1.278	15,109
4	3	12	6	4	20	1.793	0.98	0.391	1725
5	4	4	20	6	80	0.541	3.145	0.593	5664
6	1	18	16	10	40	2.906	2.589	1.001	1708
7	2	8	8	20	60	1.143	1.265	2.289	3565
8	8	14	18	18	30	2.203	2.917	2.119	4708
9	9	6	2	8	50	0.835	0.366	0.802	7356
10	7	20	10	2	70	3.191	1.563	0.298	7333

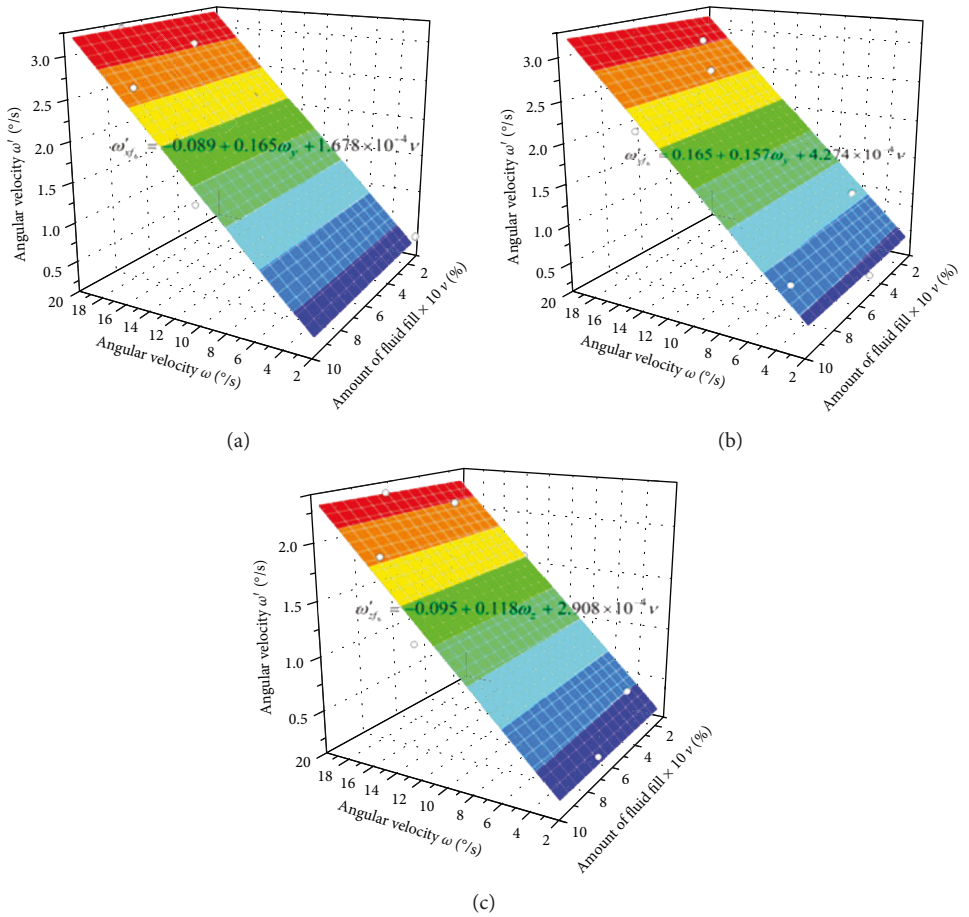

Figure 14: Fitting polynomial and surface fitting results of liquid storage tank and microsatellite with the deployment mechanism for (a) ω'_{xf_6}, (b) ω'_{yf_6}, and (c) ω'_{zf_6}.

Table 21: ω'_{xf_6}, ω'_{yf_6}, and ω'_{zf_6} of the surface regression equations.

No.	Regression equation	Multiple R
1	$\omega'_{xf_6} = -0.089 + 0.165\omega_x + 1.678 \times 10^{-4}\nu$	0.997
2	$\omega'_{yf_6} = 0.165 + 0.157\omega_y + 4.274 \times 10^{-4}\nu$	0.999
3	$\omega'_{zf_6} = -0.095 + 0.118\omega_z + 2.908 \times 10^{-4}\nu$	0.995

angular velocity of the empty storage tank and sloshing angular velocity. Furthermore, the disturbance angular velocity generated by the liquid storage tank has a surface relationship with the sloshing angular velocity and amount of the filled liquid. The two sloshing models are independent of time, and the multiple-R value of the model is larger than 0.98, indicating the validity of the model. For the three considered cases, the disturbance angular velocity of the liquid storage tank is higher than that of the empty storage tank,

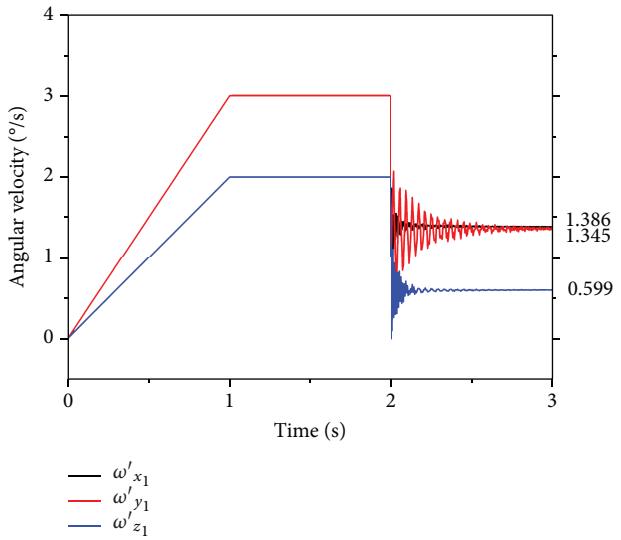

FIGURE 15: Simulation results of empty storage tank for ω'_{x_1}, ω'_{y_1}, and ω'_{z_1} when $\omega'_x = 3$, $\omega'_y = 3$, and $\omega'_z = 2$.

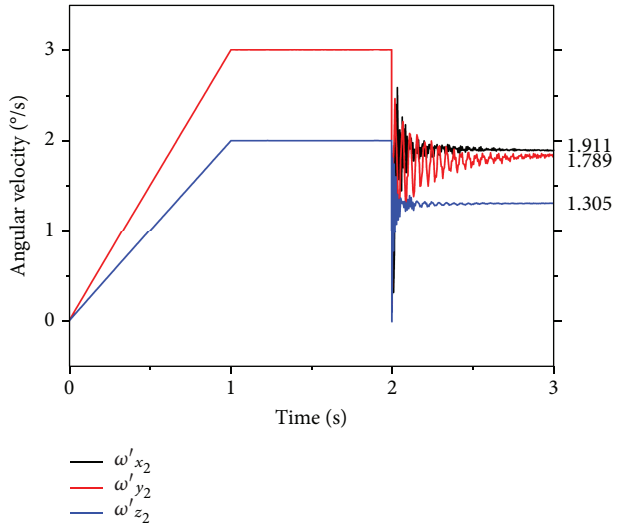

FIGURE 16: Simulation results of liquid storage tank for ω'_{x_2}, ω'_{y_2}, and ω'_{z_2} when $\omega'_x = 3$, $\omega'_y = 3$, $\omega'_z = 2$, and $\nu = 100$.

and the disturbance decreases with an increase in the mass of the coupling.

The simulation results of the three states of the storage tanks obtained when the amount of the filled liquid propellant in the storage tank and microsatellite during orbit is 100%, and the separation attitude angular velocity is satisfied according to the separation requirements are shown in Figures 15–20. Moreover, the results of the simulation analysis and errors are compared in Tables 22–24. The tables show that the maximum and minimum deviation of the three states is 7.6% and is 1.1%, respectively, which indicates that the regression model of the tank with sloshing is effective.

When the sloshing angular velocity inputs for the calculation and simulation analysis are $|\omega_x| = 3°/s$, $|\omega_y| = 3°/s$, and $|\omega_z| = 2°/s$ to generate positive results, the results of

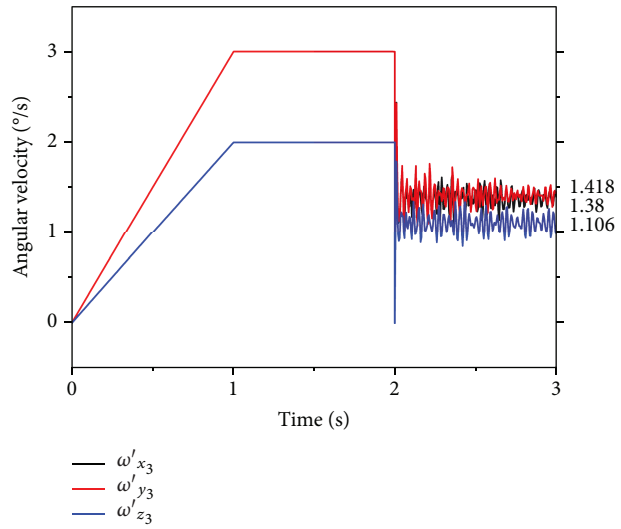

FIGURE 17: Simulation results of empty storage tank and microsatellite for ω'_{x_3}, ω'_{y_3}, and ω'_{z_3} when $\omega'_x = 3$, $\omega'_y = 3$, and $\omega'_z = 2$.

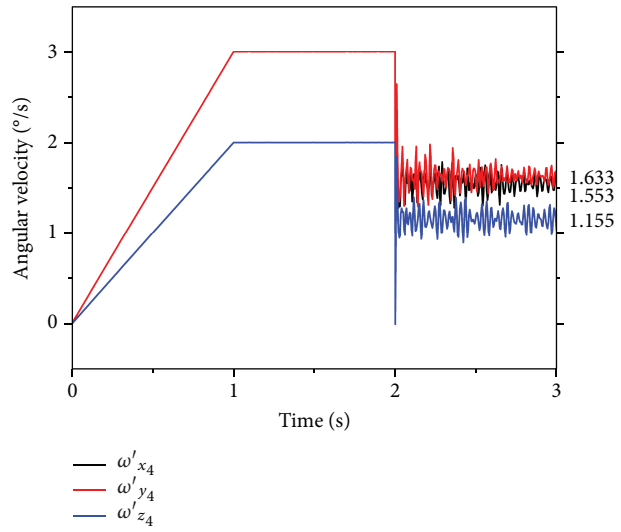

FIGURE 18: Simulation results of liquid storage tank and microsatellite for ω'_{x_4}, ω'_{y_4}, and ω'_{z_4} when $\omega'_x = 3$, $\omega'_y = 3$, $\omega'_z = 2$, and $\nu = 100$.

the calculation are $|\omega'_{xf_6}| = 0.389°/s$, $|\omega'_{yf_6}| = 0.529°/s$, and $|\omega'_{zf_6}| = 0.17°/s$, respectively, and the results of the simulation are $|\omega'_{x_6}| = 0.383°/s$, $|\omega'_{y_6}| = 0.507°/s$, and $|\omega'_{z_6}| = 0.158°/s$, respectively.

6. Results and Discussion

The Zhejiang University microsatellites are double satellites; microsatellite A is filled with a propellant, and microsatellite B is not filled with a propellant. Following the separation of the satellite from the rocket during orbit, the angular velocities of the three axes are satisfied with the separation precision listed in Table 5. Then, the deployment mechanism on the satellites is executed, and the orbit data of the entire process is relayed to the ground. The changing process of the

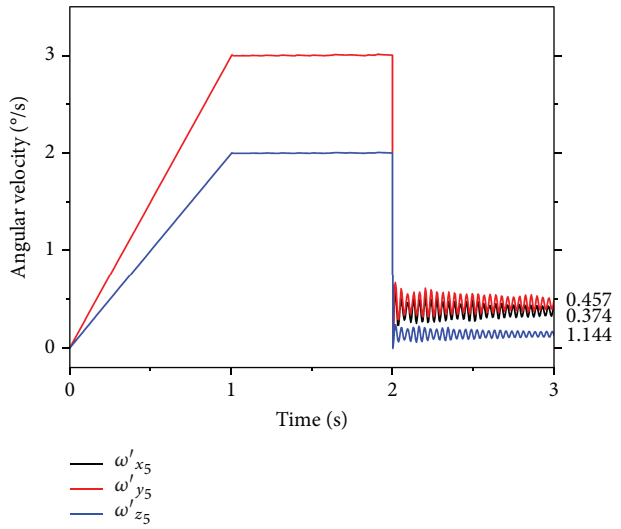

Figure 19: Simulation results of empty storage tank and microsatellite with the deployment mechanism for ω'_{x_5}, ω'_{y_5}, and ω'_{z_5} when $\omega'_x = 3$, $\omega'_y = 3$, and $\omega'_z = 2$.

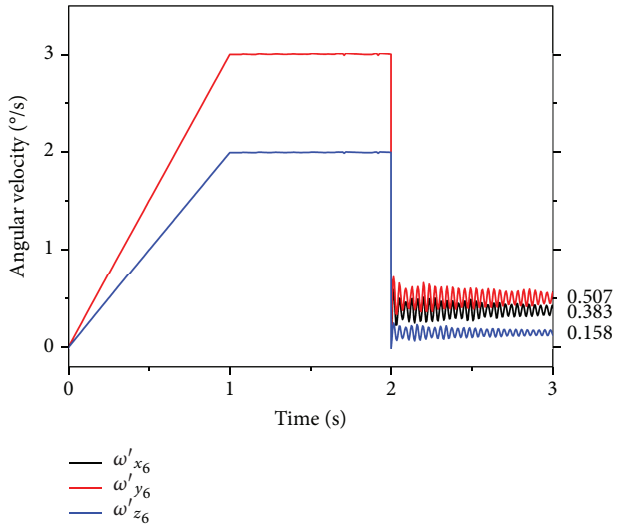

Figure 20: Simulation results of liquid storage tank and microsatellite with the deployment mechanism for ω'_{xf_6}, ω'_{yf_6}, and ω'_{zf_6} when $\omega'_x = 3$, $\omega'_y = 3$, $\omega'_z = 2$, and $\nu = 100$.

Table 22: Relative errors of calculation and simulation results for storage tank.

Calculation results	Simulation results	Relative errors
$\omega'_{xf_1} = 1.419$	$\omega'_{x_1} = 1.386$	2.4%
$\omega'_{yf_1} = 1.36$	$\omega'_{y_1} = 1.345$	1.1%
$\omega'_{zf_1} = 0.615$	$\omega'_{z_1} = 0.599$	2.7%
$\omega'_{xf_2} = 2.016$	$\omega'_{x_2} = 1.911$	5.5%
$\omega'_{yf_2} = 1.848$	$\omega'_{y_2} = 1.789$	3.3%
$\omega'_{zf_2} = 1.333$	$\omega'_{z_2} = 1.305$	2.1%

Table 23: Relative errors of calculation and simulation results for storage tank and microsatellite.

Calculation results	Simulation results	Relative errors
$\omega'_{xf_3} = 1.407$	$\omega'_{x_3} = 1.38$	1.9%
$\omega'_{yf_3} = 1.449$	$\omega'_{y_3} = 1.418$	2.2%
$\omega'_{zf_3} = 1.148$	$\omega'_{z_3} = 1.106$	3.8%
$\omega'_{xf_4} = 1.535$	$\omega'_{x_4} = 1.553$	1.2%
$\omega'_{yf_4} = 1.512$	$\omega'_{y_4} = 1.633$	7.4%
$\omega'_{zf_4} = 1.198$	$\omega'_{z_4} = 1.155$	3.7%

Table 24: Relative errors of calculation and simulation results for storage tank and microsatellite with the deployment mechanism.

Calculation results (°/s)	Simulation results (°/s)	Relative errors
$\omega'_{xf_5} = 0.379$	$\omega'_{x_5} = 0.374$	1.3%
$\omega'_{yf_5} = 0.486$	$\omega'_{y_5} = 0.457$	6.3%
$\omega'_{zf_5} = 0.138$	$\omega'_{z_5} = 0.144$	4.2%
$\omega'_{xf_6} = 0.389$	$\omega'_{x_6} = 0.383$	1.6%
$\omega'_{yf_6} = 0.529$	$\omega'_{y_6} = 0.507$	4.3%
$\omega'_{zf_6} = 0.17$	$\omega'_{z_6} = 0.158$	7.6%

attitude angular velocity is displayed in Figure 21. Figure 21 illustrates that the attitude angular velocity of the initial satellite separation is high and stable following the attitude adjustment. The angular velocity ranges for the sloshing in microsatellite A are (−0.256, 0.278), (−0.319, 0.349), and (−0.157, 0.164) and in microsatellite-B are (−0.215, 0.238), (−0.248, 0.269), and (−0.138, 0.148) for each axis.

The deviation between the calculation and experimental results is expressed by the following equation:

$$\delta_i = \frac{\left|\left|\omega'_{\text{if}}\right| - \left|\omega_i\right|\right|}{\left|\omega_i\right|} \times 100\%, \tag{18}$$

where δ_i is the deviation, $i = x, y, z$, ω'_{if} denotes the calculation results, and ω_i denotes the experimental results.

The calculation and experimental results of microsatellites A and B are summarized in Table 25, where test results A and B are calculated according to (17). Table 25 demonstrates that that the maximum disturbance deviation is in the y direction and is 43.36% whereas the minimum deviation is in the z direction and is 14.86%.

Because the disturbance angular velocity is low, there is an error between the orbital data and calculation results. This deviation is mainly caused by the simplification of the model, precision of the model, precision of the attitude sensor, and unfolding of the deployment mechanism. However, the calculation results can reflect the trends of the

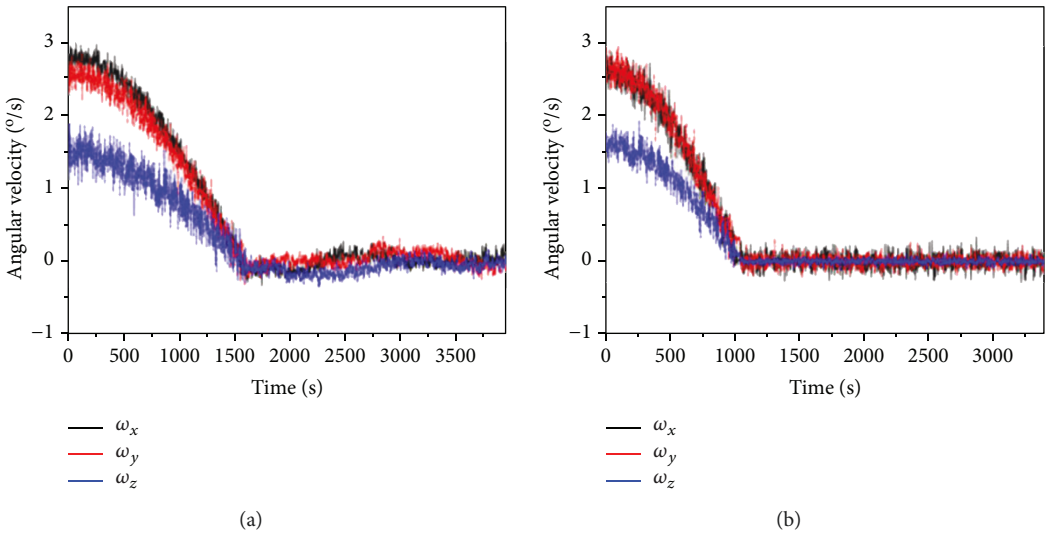

Figure 21: Angular velocity of on orbit attitude of Zhejiang University microsatellites: (a) A satellite and (b) B satellite.

Table 25: The comparison of calculation and test results.

Technical specification	Calculation results-A	Calculation results-B	Test results-A	Test results-B	Relative errors-A	Relative errors-B
Rolling angular velocity (°/s)	0.138	0.17	0.164	0.148	15.85%	14.86%
Pitch velocity (°/s)	0.379	0.389	0.278	0.338	36.33%	15.09%
Yaw velocity (°/s)	0.486	0.529	0.349	0.369	39.25%	43.36%

satellite disturbance state and attitude angular velocity of the satellite during orbit. The effect of the initial angular velocity and liquid sloshing on the satellite attitude angular velocity is consistent with the calculation results. This effect is small and of the order of 10^{-2}°/s when the angular velocities of the satellite are $\omega_x' = 3$, $\omega_y' = 3$, and $\omega_z' = 2$.

The satellite propellant weight accounts for 0.03% of the entire satellite weight, and the magnitude of the attitude disturbance angular velocity is 10^{-2}°/s. This indicates that the disturbance of the attitude angular velocity of a microsatellite is directly determined by the liquid propellant volume. Thus, the results can be extended to larger satellites, and a quantitative evaluation of the angular velocity of the disturbance derived from sloshing can be obtained. For microsatellite formations and satellites that require high-precision attitude positioning, such as those acquiring photographs and videos, the effect of the disturbance angular velocity of the propellant cannot be ignored. Therefore, it is necessary to improve the accuracy of the liquid-sloshing model and generate a mixture model that considers the gas–liquid two-phase mixture of the propellant. Furthermore, this will help predict the disturbance angular velocity and provide the high-precision and real-time adjustment of the momentum wheel for restraining the satellite attitude disturbance. The method of increasing the structure of the storage tank to prevent liquid sloshing without affecting the tank performance of the propulsion system can also restrain the attitude disturbance. This complex network structure, generated by 3D printing, has been mentioned in the literature [22].

7. Conclusions

In this study, a method for establishing the prediction model of the liquid-sloshing characteristics of a microsatellite propulsion system is proposed. The ideal states of the liquid-sloshing characteristics are considered for three cases. The relationship models between the sloshing time, sloshing angular velocity, amount of fluid filled, and satellite attitude angular velocity are established. The analysis results show that the disturbance angular velocity of the empty storage tank and sloshing angular velocity have a linear relationship. Furthermore, the disturbance angular velocity of the liquid storage tank demonstrates a surface relationship with the sloshing angular velocity and amount of fluid filled. Additionally, the disturbance angular velocity for the liquid state of the storage tank is higher than that for the empty state, and the degree of disturbance decreases with increase in the mass of the coupling. The disturbance of the storage tank and satellite with the deployment mechanism is 10^{-2}°/s when the angular velocities of the satellite are $\omega_x' = 3$, $\omega_y' = 3$, and $\omega_z' = 2$. The maximum deviation between the calculation and simulation results of the three models is 7.6%, and the minimum deviation is 1.1%. The model is used to predict the disturbance angular velocity of the microsatellite. When compared with the orbital satellite data, the maximum disturbance angular velocity deviation of 43.36% occurs in the y direction, whereas the minimum deviation of 14.86% occurs in the z direction, which demonstrates the accuracy of the analysis and model.

Data Availability

The data used to support the findings of this study are available from the corresponding author upon request.

Conflicts of Interest

The authors declare that they have no conflicts of interest.

Acknowledgments

This research was funded by the China National Funds for Distinguished Young Scientists (grant number 61525403) and Fundamental Research Funds for the Central Universities (grant number 2017QNA4035).

References

[1] X. L. Ling, "Micro-propulsion system for modern small satellites," *Spacecraft Engineering*, vol. 19, no. 6, pp. 13–20, 2010.

[2] M. Ihmsen, J. Cornelis, B. Solenthaler, C. Horvath, and M. Teschner, "Implicit incompressible SPH," *IEEE Transactions on Visualization and Computer Graphics*, vol. 20, no. 3, pp. 426–435, 2014.

[3] H. Zhang, *Research on Fluid Movement and Solid-Fluid Coupling Simulation Based on SPH*, Master's Thesis, University Of Science and Technology of China, Hefei, China, 2015.

[4] G. X. Ni, R. L. Wang, Z. Lin, and Q. W. Ge, "Equi-distribution of particles in arbitrary domain," *Chinese Journal of Computational Mechanics*, vol. 24, no. 4, pp. 408–413, 2007.

[5] M. B. Liu and J. Z. Chang, "Particle distribution and numerical stability in smoothed particle hydrodynamics method," *Acta Physica Sinica*, vol. 59, no. 6, pp. 3654–3662, 2010.

[6] R. A. Gingold and J. J. Monaghan, "Smoothed particle hydrodynamics: theory and application to non-spherical stars," *Monthly Notices of the Royal Astronomical Society*, vol. 181, no. 3, pp. 375–389, 1977.

[7] L. B. Lucy, "A numerical approach to the testing of the fission hypothesis," *The Astronomical Journal*, vol. 82, pp. 1013–1024, 1977.

[8] J. J. Monaghan, "Simulating free surface flows with SPH," *Journal of Computational Physics*, vol. 110, no. 2, pp. 399–406, 1994.

[9] M. R. Jiang, B. Ren, H. J. Wen, and Y. X. Wang, "Experimental study on sloshing in elastic tanks," *Ocean Engineering*, vol. 31, no. 5, pp. 1–10, 2013.

[10] M. Liu, R. Zhou, and J. Shao, "Numerical simulation of liquid sloshing in aprismatic tank with SPH method," *Journal of Hohai University*, vol. 42, no. 3, pp. 257–261, 2014.

[11] Y. T. Hang, F. X. Du, H. Liu, J. Wang, Z. C. Ou, and X. H. Yao, "Analysis on sloshing characteristics of liquid in elastomer tank based on SPH method," *Computer Aided Engineering*, vol. 24, no. 2, pp. 36–41, 2015.

[12] T. Hao, X. Jian, and Z. Jianhui, "Study of liquid sloshing in missile fuel tank based on SPH method," *Wireless Internet Technology*, vol. 3, pp. 76–79, 2015.

[13] F. L. Cardoso-Ribeiro, D. Matignon, and V. Pommier-Budinger, "A port-Hamiltonian model of liquid sloshing in moving containers and application to a fluid-structure system," *Journal of Fluids and Structures*, vol. 69, pp. 402–427, 2017.

[14] S. M. Hasheminejad and H. Soleimani, "An analytical solution for free liquid sloshing in a finite-length horizontal cylindrical container filled to an arbitrary depth," *Applied Mathematical Modelling*, vol. 48, pp. 338–352, 2017.

[15] B. Nicolsen, L. Wang, and A. Shabana, "Nonlinear finite element analysis of liquid sloshing in complex vehicle motion scenarios," *Journal of Sound and Vibration*, vol. 405, pp. 208–233, 2017.

[16] M. Farid and O. V. Gendelman, "Response regimes in equivalent mechanical model of strongly nonlinear liquid sloshing," *International Journal of Non-Linear Mechanics*, vol. 94, no. 4, pp. 146–159, 2017.

[17] H. Hang, L. Yang, H. Zhang, and G. J. Qu, "Three dimensional centroid surface equivalent model for large liquid sloshing in spacecraft tank," *Journal Astronautics*, vol. 31, no. 1, pp. 55–59, 2010.

[18] S. Ahmad and B. Yue, "Motion stability dynamics for spacecraft coupled with partially filled liquid container," *Theoretical and Applied Mechanics Letters*, vol. 2, no. 1, article 013002, 2012.

[19] M. Lazzarin, M. Biolo, A. Bettella, M. Manente, R. da Forno, and D. Pavarin, "EUCLID satellite: development of a lumped parameter model for sloshing description," *Aerospace Science and Technology*, vol. 39, pp. 491–500, 2014.

[20] Z. Zhou and H. Huang, "Constraint surface model for large amplitude sloshing of the spacecraft with multiple tanks," *Acta Astronautica*, vol. 111, pp. 222–229, 2015.

[21] M. Chiba and H. Magata, "Influence of liquid sloshing on dynamics of flexible space structures," *Journal of Sound and Vibration*, vol. 401, pp. 1–22, 2017.

[22] L. Teng and Z. Jin, "Structural performance optimization and verification of an improved thin-walled storage tank for a Pico-satellite," *Applied Sciences*, vol. 7, no. 11, p. 1168, 2017.